energies

Study Protocol

Site Selection and Capacity Determination of Electric Hydrogen Charging Integrated Station Based on Voronoi Diagram and Particle Swarm Algorithm

Xueqin Tian [1,2], Heng Yang [2,*], Yangyang Ge [3] and Tiejiang Yuan [2]

[1] China Electric Power Research Institute Co., Ltd., Haidian District, Beijing 100192, China; tianxueqin@chinasperi.sgcc.com.cn
[2] School of Electrical Engineering, Dalian University of Technology, Dalian 116024, China; ytj1975@dlut.edu.cn
[3] Electric Power Research Institute of State Grid Liaoning Electric Power Co., Ltd., Shenyang 110006, China; 15942302722@163.com
* Correspondence: yh782459245@mail.dlut.edu.cn

Abstract: In response to challenges in constructing charging and hydrogen refueling facilities during the transition from conventional fuel vehicles to electric and hydrogen fuel cell vehicles, this paper introduces an innovative method for siting and capacity determination of Electric Hydrogen Charging Integrated Stations (EHCIS). In emphasizing the calculation of vehicle charging and hydrogen refueling demands, the proposed approach employs the Voronoi diagram and the particle swarm algorithm. Initially, Origin–Destination (OD) pairs represent car starting and endpoints, portraying travel demands. Utilizing the traffic network model, Dijkstra's algorithm determines the shortest path for new energy vehicles, with the Monte Carlo simulation obtaining electric hydrogen energy demands. Subsequently, the Voronoi diagram categorizes the service scope of EHCIS, determining the equipment capacity while considering charging and refueling capabilities. Furthermore, the Voronoi diagram is employed to delineate the EHCIS service scope, determine the equipment capacity, and consider distance constraints, enhancing the rationality of site and service scope divisions. Finally, a dynamic optimal current model framework based on second-order cone relaxation is established for distribution networks. This framework plans each element of the active distribution network, ensuring safe and stable operation upon connection to EHCIS. To minimize the total social cost of EHCIS and address the constraints related to charging equipment and hydrogen production, a siting and capacity model is developed and solved using a particle swarm algorithm. Simulation planning in Sioux Falls city and the IEEE33 network validates the effectiveness and feasibility of the proposed method, ensuring stable power grid operation while meeting automotive energy demands.

Keywords: electric vehicles; hydrogen fuel cell vehicles; site selection and fixed capacity; Voronoi diagram; electric hydrogen charging integrated station

check for updates

Citation: Tian, X.; Yang, H.; Ge, Y.; Yuan, T. Site Selection and Capacity Determination of Electric Hydrogen Charging Integrated Station Based on Voronoi Diagram and Particle Swarm Algorithm. *Energies* **2024**, *17*, 418. https://doi.org/10.3390/en17020418

Academic Editor: Giovanni Lutzemberger

Received: 23 November 2023
Revised: 23 December 2023
Accepted: 9 January 2024
Published: 15 January 2024

1. Introduction

With the large-scale use of fuel vehicles, the environmental problems caused by them have gradually attracted people's attention. In order to reduce carbon emissions and realize low-carbon environmental protection from traditional fuel vehicles, it is imperative to promote the application of new energy vehicles [1]. New energy vehicles mainly include electric vehicles and hydrogen fuel cell vehicles [2].

Hydrogen energy, as a green energy source, will play a significant role in upgrading and transforming traditional fuel vehicles and realizing a low-carbon process. Due to the actual factors, such as the power grid structure, vehicle energy storage capacity, and replenishment method, there are significant differences between the siting and sizing of EHCIS and the traditional fuel vehicle refueling station site: the large-scale centralized charging of electric vehicles will impact the power grid, affecting the frequency and voltage stability, and compared with the short-term refueling of fuel vehicles, the charging of electric vehicles takes a long time, so a reasonable site layout of the charging station is needed to avoid the centralized charging of electric vehicles. With the increasing proportion of new energy vehicles, it is of great significance to carry out a study on the location and capacity of EHCIS in order to meet the energy demand of electric vehicles (EV) and hydrogen fuel cell vehicles (HFCV).

For the planning study of EHCIS, firstly, the planning methodology of the charging station can be borrowed. In [3], on the basis of candidate charging station sites, charging stations are planned with the objective of minimizing the distance traveled by cars to the charging station. This approach meets the energy demand of electric vehicles but ignores the influence of roads on the car's driving behavior. In [4], the charging station planning model is established with the objective of minimizing the cost of charging station construction and management as well as the cost of EV driving losses, but it is specific in that it considers the airport road as a one-dimensional road. In [5], considering the influence of a transportation road network on electric vehicle charging demand, a two-stage method is used, in which the first stage obtains the spatial and temporal distribution of automobile electric energy demand, and the second stage establishes a model for optimal siting and capacity determination of charging stations with the objective of minimizing charging station operation and investment costs. Secondly, the planning methodology for hydrogen refueling stations can be drawn upon. In [6], the authors propose a hydrogen network supply system for wind power generation, and the model can be used for hydrogen refueling station planning and provides a rational hydrogen infrastructure layout scheme. In [7], the authors propose a hydrogen refueling site sizing model based on the life cycle cost of hydrogen, yet only a one-dimensional highway is used as the study object, which does not have the two-dimensional characteristics of the urban transportation plane. In [8], the authors propose to establish a cross-regional transportation fuel cell vehicle hydrogen refueling station siting model based on the traffic flow capture model, which takes into account the average road vehicle speed, the road traffic flow, the maximum vehicle mileage, and the maximum number of hydrogen refueling stations constructed to obtain the hydrogen refueling station siting scheme between different regions.

Finally, for the study of an EHCIS, the authors [9] propose a market-based power purchase strategy for EHCIS based on peak shaving and valley filling, wind and solar energy consumption, and hydrogen energy supply and verify that the integrated station effectively improves the capacity of peak shaving and valley filling and new energy consumption of the power grid. In [10], sampling is conducted on the basis of four uncertainties: wind, light, electricity, and hydrogen to demonstrate the economy and effectiveness of capacity planning for EHCIS under different scenarios.

In summary, the existing research focuses on the location and capacity of individual EV charging stations or HFCV refueling stations without considering the driving characteristics of EVs and HFCVs in the city, the lack of a simultaneous supply of electricity and hydrogen and the lack of related equipment capacity planning, and the lack of research on the large-scale access to the grid for EVs and HFCVs.

This paper proposes a planning method for EHCIS to meet the energy demand of EVs and HFCVs. The main contributions of this paper are as follows:

(1) The OD travel matrix is used to portray the transportation demand, and then Dijkstra's algorithm is used to plan the shortest driving paths of the vehicles to calculate the electric energy demand of EVs and the hydrogen energy demand of HFCVs.
(2) The Voronoi diagram is used to divide the service area of each EHCIS site and determine the equipment capacity of the EHCIS.
(3) Finally, simulation planning using the city of Sioux Falls and the IEEE33 network ensures stable operation of the grid while meeting the energy demand of EVs and HFCVs.

2. Framework for the Operation of EHCIS

This paper proposes an EHCIS, which refers to a place to provide hydrogen energy for EVs and HFCVs, as illustrated in Figure 1. Due to the rapid development of the hydrogen energy system [11], the electric hydrogen manufacturing and charging station can realize the energy management of the distribution grid, distributed energy, hydrogen manufacturing, and storage on the source side and realize the coordination and optimization of EVs and HFCVs on the load side to achieve the purpose of energy saving and emission reduction in transportation.

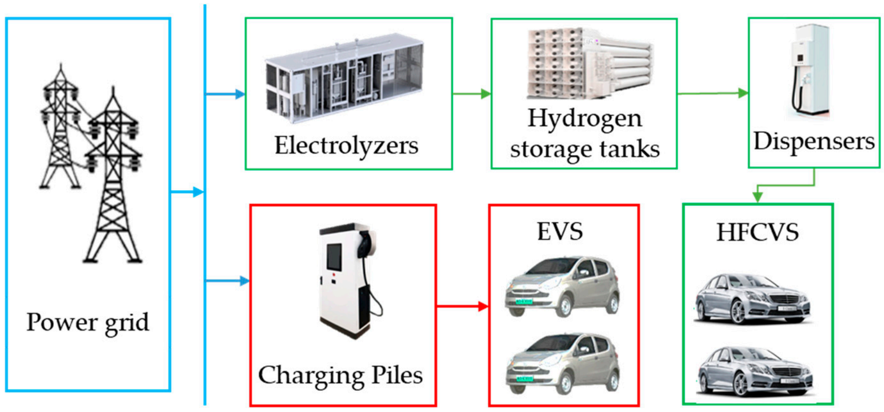

Figure 1. Framework for the operation of EHCIS.

The evolution of power electronics technology plays a crucial role in the realm of Electric Vehicle (EV) charging stations, addressing key challenges related to charging efficiency, sustainability, and environmental considerations. Reference [12] underscores the pivotal role of Solid State Transformer (SST) technology. By integrating advanced power electronics and enabling the connection of two independent power grids through isolation, SST is deemed the leading solution for adapting to changes in power network architectures. Its widespread application in smart grids, data centers, railways, and offshore wind farms highlights its promising prospects. This paper emphasizes the critical role of SST technology in supporting energy transition and the development of advanced smart grids. In [13], the research involves a real-world application of a 50-kW Vehicle-to-Grid (V2G) charging station. Employing SiC semiconductors for enhanced efficiency and power density, the station integrates AC/DC and DC/DC converters to provide V2G charging points with grid stabilization capabilities. The success of this design application on Madeira Island demonstrates its feasibility, establishing a reliable charging infrastructure for electric vehicles within island microgrids.

In [14], an emphasis is placed on the design and power management of a charging station integrating solar power and a Battery Energy Storage System (BESS). Through strategies such as Maximum Power Point Tracking (MPPT), Proportional-Integral-Derivative (PID) control, and current control, the station achieves optimal power distribution between solar, BESS, and the grid, catering to dynamic EV charging needs. The proposed solution offers a promising approach to satisfying the charging requirements of electric vehicles connected throughout the day, making use of PID, current control, and voltage control to maintain constant DC bus voltage for the station. A conclusion can be drawn that the development of power electronics technology in electric vehicle charging stations not only enhances the charging efficiency but also supports the stability of the grid and the integration of renewable energy sources. This provides critical technological support for the promotion of electric vehicles and the application of sustainable energy.

An electric vehicle fast charging device realizes the fast charging of EVs [15]. A hydrogen energy system includes a hydrogen production unit, a hydrogen storage unit, and a hydrogen refueling unit. A hydrogen production device consists of an electrolyzer, which electrolyzes water through electrodes to obtain hydrogen and oxygen. At the present stage, the hydrogen production project mainly adopts a proton exchange membrane and an alkaline electrolyzer, which is highly flexible and adaptable. It can operate stably and safely at high current density and low voltage. In this paper, an alkaline electrolyzer is used to produce hydrogen with a high-pressure gaseous storage hydrogen tank [16].

3. Automotive Electric Hydrogen Demand Model

EVs consume electric energy while traveling, and the corresponding HFCVs consume hydrogen energy. The calculation and simulation of the energy demand of EVs and HFCVs is the basis for the siting and capacity determination of the EHCIS.

3.1. Transportation Network Model

The transportation network is an important carrier of new energy vehicle driving [17], and its topology has an important impact on the driving path of new energy vehicles. Through the graph theory [18], the transportation road network model can be established to portray the characteristics of the road network. Figure 2 shows the topology of the transportation road network.

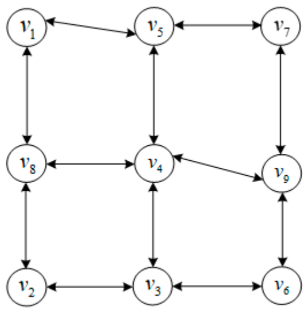

Figure 2. Traffic network topology.

The mathematical description of the transportation road network is shown in Equation (1) [19]:

$$\begin{aligned} & G = (V, E, K, W) \\ & V = \{v_i | i = 1, 2, 3, \cdots, n\} \\ & E = \{v_{ij} | v_i \in V, v_j \in V, i \neq j\} \\ & K = \{k | k = 1, 2, 3, \cdots, m\} \\ & W = \left\{w_{ij}^k \middle| v_{ij} \in E, k \in K\right\} \end{aligned} \tag{1}$$

where G is the traffic network; V denotes the traffic intersection; E denotes the traffic section; W is the roadway resistance; and K denotes the m time periods throughout the day.

The structure of the traffic road network in Figure 2 is represented using the adjacency matrix A, as demonstrated in Equation (2) [20]:

$$A = \begin{bmatrix} A_{11} & A_{12} & \cdots & A_{1N} \\ A_{21} & A_{22} & \cdots & A_{2N} \\ \vdots & \vdots & \ddots & \vdots \\ A_{M1} & A_{M2} & \cdots & A_{MN} \end{bmatrix} \tag{2}$$

The assignment rule for the element A_{ij} in matrix A is as Equation (3) [20]:

$$A_{ij} = \begin{cases} w_{ij}, & v_{ij} \in E \\ 0, & v_i = v_j \\ \text{inf}, & v_{ij} \notin E \end{cases} \tag{3}$$

where inf denotes that there is no directly connected road section between node v_i and v_j, and w_{ij} denotes the road resistance from node v_i to v_j.

Considering the fact that users are actually more concerned about the car traveling time while driving [21], this study chooses the car travel time as a characterization of roadway resistance for modeling and analysis.

3.2. New Energy Vehicle Charging and Hydrogen Injection

3.2.1. Road Resistance Function

When making a path selection, the route with the shortest traveling time is preferred. In order to reflect the relationship between the traffic time and the density of each road segment and other factors, this paper adopts the road resistance function method. The road resistance function is often calculated according to the following formula, calculated by Equation (4) [22]:

$$T_{at}(x_{at}) = T_{at}^{0}[1 + \alpha(x_{at}/C_a)^{\beta}] \tag{4}$$

where T_{at}^{0} denotes the free passage time of section α; C_a is the capacity of line α; x_{at} denotes the flow rate of section a at time t; and $\alpha = 0.15$, $\beta = 4$.

3.2.2. Vehicle Path Planning

In order to simulate the travel demand of EVs and HFCVs, the OD matrix representation of traffic origins and destinations is used [23], and (m, n) is defined as an OD pair, where m denotes the user's starting point, n denotes the ending point, and M denotes the set of OD pairs, as shown in Equation (5).

$$M = \begin{bmatrix} M_{11} & M_{12} & \cdots & M_{1n} \\ M_{21} & M_{22} & \cdots & M_{2n} \\ \vdots & \vdots & \ddots & \vdots \\ M_{m1} & M_{11} & \cdots & M_{mn} \end{bmatrix} \tag{5}$$

where M_{mn} is the traffic flow from intersection m to intersection n.

3.2.3. EV Electricity Demand and HFCV Hydrogen Demand Calculation

(1) First, we obtain urban traffic information, including the traffic network structure and road resistance, and read the travel demand of EVs and HFCVs, including the travel moments, starting points and ending points of EVs and HFCVs, the initial power quantity of EVs, and the initial hydrogen quantity of HFCVs. State parameters for EVs $EV = \{EO_i, ED_i, Et_s, EL_t, ECap_r\ \ ECap_0, ECap_t, E\Delta cap\}$; state parameters for HFCVs $HFCV = \{FO_i, FD_i, Ft_s, FL_t, FCap_r, FCap_0, FCap_t, F\Delta cap\}$. The meaning of each parameter is shown in Table 1.

Table 1. Car state parameters.

Parameter	Explanation	Parameter	Explanation
EO_i	EV Starting Point	Et_s	EV travel time
ED_i	EV Endpoints	EL_t	Position of the EV at time t
$ECap_r$	EV Capacity	$ECap_0$	Initial power of EV
$ECap_t$	Amount of power remaining in the EV at time t	$E\Delta cap$	Consumption per kilometer Electricity consumption
FO_i	HFCV starting point	FD_i	HFCV endpoint
Ft_s	HFCV position at time t	FL_t	HFCV position at time t
$FCap_r$	HFCV hydrogen content	$FCap_0$	Initial hydrogen for hydrogen
$FCap_t$	Amount of hydrogen remaining in the HFCV at time t	$F\Delta cap$	Hydrogen consumption per kilometer

In this paper, we use the probability distribution curves of the initial travel moments and return moments of cars on a typical weekday provided in the literature [24] to generate the initial travel moments of EVs and HFCVs. We assume [25] that the initial power of each EV and the initial hydrogen energy distribution of the HFCVs satisfy the normal distribution $N(0.5, 0.1^2)$.

(2) Complementary energy demand judgment and user decision-making

After the vehicle has traveled to a certain intersection [26], the user determines whether it needs to replenish energy to travel to the destination based on the remaining power and hydrogen of the vehicle. In this paper, it is assumed that if the EV's power or HFCV's hydrogen amount is less than 20% or the remaining energy of the car is not enough to reach the destination, the car needs to go to the charging station at the current intersection to replenish the energy. When the car continues to its destination after refueling, the cost of the loss between the car and the EHCIS will be calculated as part of the planning cost of the EHCIS, according to Equation (6).

$$\zeta_i^s = \begin{cases} 1 & S(i_s) \leq 20\% \text{ or } L_R(i_s) \leq L_{s,D} \\ 0 & \text{other} \end{cases} \tag{6}$$

where the ζ_i^s function determines whether the ith car needs to be charged and injected with hydrogen when it travels to s, 1 indicates that the car needs to be replenished, and 0 indicates that it does not need to be replenished; $S(i_s)$ is the remaining energy of the car when it arrives at the intersection s; $L_R(i_s)$ is the mileage that can be traveled with the remaining power and hydrogen in kilometers; and $L_{s,D}$ is the distance between the current intersection node s and the destination in kilometers.

(3) Based on Dijkstra's shortest-path planning

Dijkstra's algorithm is suitable for graphs without negative edge weights. In road networks, where edge weights typically represent distances or travel times, these values are non-negative [27]. This makes Dijkstra's algorithm well-suited to finding the shortest paths in road networks. Dijkstra's algorithm is generally faster in sparse graphs compared to the Bellman–Ford algorithm and the road networks tend to be sparse. The time complexity of Dijkstra's algorithm is O ((*V* + *E*) log *V*) [28], while the Bellman–Ford algorithm has a time complexity of O (*VE*). In road networks, where *V* may represent intersections and E may represent road segments, E is often much smaller than *V*. Dijkstra's algorithm is usually faster for graphs with positive weights, especially in the case of dense graphs or small weight values, whereas the Bellman–Ford algorithm is more general and is able to handle graphs containing negative weights, and the Bellman–Ford algorithm is relatively slow. In this paper, the weight of urban road traffic is road resistance, and the value is positive, so compared with the Bellman–Ford algorithm, this paper adopts Dijkstra's algorithm, which is more appropriate.

After the EV and HFCV obtain the traveling OD pair, in order to obtain the shortest driving path planned by the EV and HFCV users, this paper adopts Dijkstra's algorithm to guide the users on the path [29], which takes the shortest driving path as the searching goal by filtering and comparing the road paths. The shortest path search is performed according to Equations (7) and (8) [30].

$$S_{ij} = \sum_{v_{ij} \in E} \left[v_{ij} w_{ij}^k(t) \right] \tag{7}$$

$$v_{ij} = \begin{cases} 1, & v_{ij} \in d_m(i) \\ 0, & v_{ij} \notin d_m(i) \end{cases} \tag{8}$$

where $v_{ij} = 1$ indicates that the road from node i to node j is in the actual traveling path $d_m(i)$, otherwise it is 0; therefore, the starting point $O(i)$ and the ending point $D(i)$, as well as the initial traveling moment $t_0(i)$ and the returning moment $t_d(i)$, are obtained through the OD travel matrix, and the traveling path is planned by Dijkstra's algorithm; dm simulates the vehicle EV/HFCV traveling route.

(4) Calculation of electric hydrogen demand

The driving paths and replenishment needs of all EVs and HFCVs in the planning area are modeled according to the aforementioned method, and the charging and hydrogen injection quantities of all EVs and HFCVs in a day are superimposed and calculated to obtain the electric hydrogen demand of all EVs in the planning area. The flow chart for total demand calculation is shown as Figure 3:

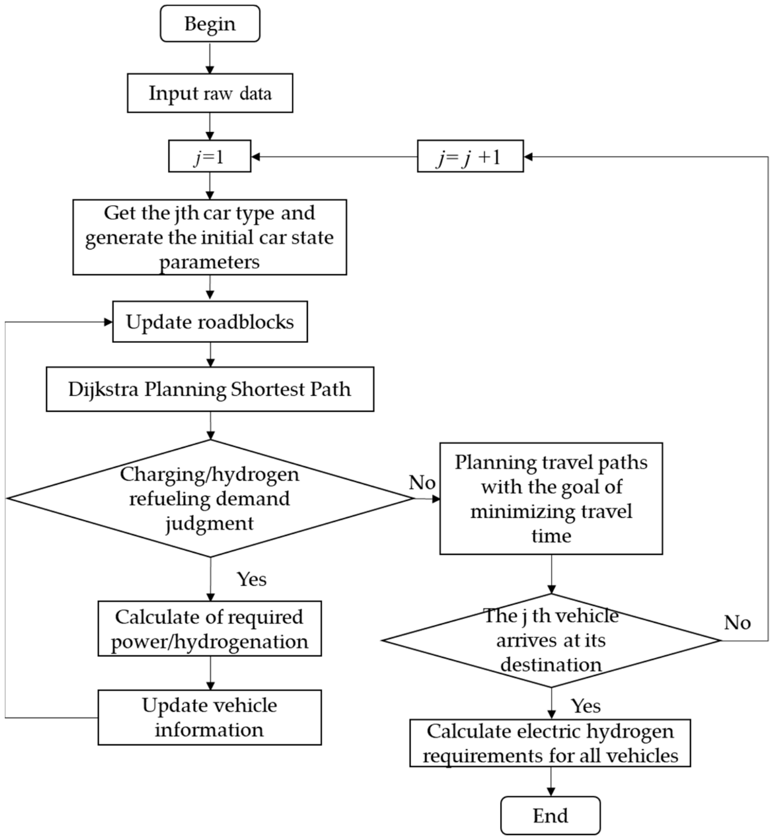

Figure 3. Calculation flow chart of hydrogen injection load for vehicle charging.

The demand for electric and hydrogen energy for EVs and HFCVs in the urban planning area sets the stage for the site selection and capacity of the EHCIS.

4. Site Selection for Capacity Determination Based on Voronoi Diagram with Particle Swarm Algorithm

4.1. The Steps for Selecting the Initial Site for EHCIS

(1) Calculate the electric and hydrogen energy demand of automobiles at each transportation node;
(2) Randomly generate N EHCIS site coordinates in the planning area and compile them as the initial particle X;
(3) Generate a Voronoi diagram [31] with each initial station site as a growth kernel, and the area formed by the growth is the service area of each charging station;
(4) Using the investment and construction cost of the EHCIS and the user's refueling loss cost as the site selection and capacity model, the particle swarm algorithm determines the optimal site distribution.

4.2. Voronoi Diagram Based on the Division of the Scope of Service of the Electric Hydrogen Refueling Integrated Station

The division of the service area of EHCIS is a prerequisite for realizing the capacity allocation of EHCIS. The Voronoi diagram, also known as the Tyson polygon or Dirichlet diagram, consists of a set of consecutive polygons consisting of perpendicular bisectors connecting the straight lines of the two neighboring points. The EHCIS is a generating element and creates vertical bisectors connecting the line segments; the intersection line between these vertical bisectors will form some polygons so that the whole plane is divided into some sub-areas through the Voronoi diagram divided into each area to establish an EHCIS when the car energy is insufficient to drive to the charging station to replenish the energy in a timely manner.

Let the set of vertices in the $P = \{p_1, p_2, \ldots, p_n\}, 3 \le n \le \infty, d(p_i, p_j)$ be the Euclidean distance between vertices p_i and p_j. The Voronoi diagram is defined as Equation (9) [32]:

$$V(p_i, \lambda_i) = \{x \in V(p_i, \lambda_i) | d(x, p_i) \le d(x, p_j)\}, \quad j = 1, 2, \cdots, n, j \ne i \tag{9}$$

The Voronoi diagram divides the plane into n regions, and each vertex in P corresponds to a $V(p_i, \lambda_i)$ region. When the car needs to replenish energy, it drives to the nearest EHCIS, and its service range is determined by the Voronoi diagram.

5. Siting and Capacity Modeling of an EHCIS

The Hydrogen Charging Station supplies energy to both EVs and HFCVs. The station includes transformers, charging piles, electrolysis tanks, hydrogen storage tanks, hydrogen dispensers, and other equipment and uses alkaline electrolyzed water to produce hydrogen in the station. Among them, the charging piles are used to replenish the energy of EVs, while the electrolysis tank, hydrogen storage tank, and hydrogen dispenser are used to produce hydrogen and dispense hydrogen to HFCVs [33].

5.1. Objective Function

The objective function for the construction of an EHCIS, which is a transportation infrastructure that provides services to users for travel, is the cost of constructing an EHCIS over the entire planning period discounted to the annual cost, and the total cost includes non-energy costs C_{1i}, C_{2i} and energy costs C_{3i}, C_{4i}:

$$\min C = \sum_{i=1}^{N} (C_{1i} + C_{2i} + C_{3i} + C_{4i}) \tag{10}$$

where C is the cost of constructing EHCIS over the entire planning period discounted to each year; N is the number of EHCIS. The individual costings are shown below:

(1) C_{1i} is the annual cost of the investment in the construction of the EHCIS:

$$C_{1i} = \frac{r_0(1+r_0)^z}{(1+r_0)^z - 1} \left(\begin{array}{l} e_i a_1 + u_i b_1 + v_i b_2 + \\ h_i c_2 + w_i d_2 + c_i \end{array} \right) \tag{11}$$

where e_i is the number of transformers in the EHCIS; a_1 is the unit price of the transformers; u_i is the number of charging piles in the EHCIS; b_1 is the unit price of the charging piles in the EHCIS; v_i is the number of hydrogen dispensers in the EHCIS; b_2 is the unit price of the hydrogen dispensers in the EHCIS; h_i is the capacity of the hydrogen tanks in the EHCIS; c_2 is the price per unit of the hydrogen tanks in the EHCIS; w_i is number of electrolyzers in the EHCIS i; d_2 is unit price of electrolyzers in the EHCIS; c_i is the capital cost of the EHCIS i; r_0 is the discount rate; and z is the operating life of the EHCIS i.

(2) The maintenance cost C_{2i} of the EHCIS consists mainly of the cost of repairing the equipment of the EHCIS and the cost of labor for the personnel. The maintenance cost is calculated as a percentage of the construction cost, with a scaling factor of η. The annual maintenance cost of the EHCIS i will be:

$$C_{2i} = \eta \left(\begin{array}{l} e_i a_1 + u_i b_1 + v_i b_2 + \\ h_i c_2 + w_i d_2 + c_i \end{array} \right) \tag{12}$$

(3) C_{3i} is the cost of purchasing electricity for the EHCIS i and the cost of electricity consumption for hydrogen production in the electrolyzer:

$$C_{3i} = \sum_{t=1}^{T} \left(P_{i,t,cd}^{sum} + P_{i,t,\text{elec}}^{sum} \right) \times p_{t,0} \tag{13}$$

where $p_{t,0}$ is the purchased electricity price of the EHCIS in time period t; $P_{i,cd}^{sum}$ is the sum of the electricity required by the charging piles in the service area of the EHCIS; and $P_{i,\text{elec}}^{sum}$ is the sum of the electricity consumed by the electrolyzer for hydrogen production.

(4) C_{4i} is the cost of the idling energy loss incurred by the user during the journey to the electric hydrogen refueling integrated station, which is expressed as a function of

$$C_{4i} = \frac{\sum L_{i,ev}}{g_{ev}} \times p_0 + \frac{\sum L_{i,hev}}{g_{hev}} \times h_0 \tag{14}$$

where $\sum L_{i,ev}$ and $\sum L_{i,hev}$ are the combined distances from all the traffic intersections within the service area of EHCIS i to the EVs and HFCVs at EHCIS i, respectively and g_{ev} and g_{hev} are the electricity and hydrogen consumed per kilometer by the EVs and HFCVs, respectively.

5.2. Determination of the Number of Hydrogen Dispensers for Charging Piles at EHCIS

If in time period t, there are n_i demand points within the service area of the EHCIS i, the number of charging piles and hydrogen dispensers in the EHCIS is configured as follows:

Number of charging piles:

$$u_i = \left\lceil \frac{\sum_{j=1}^{n_i} q_{ev,t}{}^{j} (\rho_1 + 1)}{P_1 k_{1,x}} \right\rceil \tag{15}$$

Number of hydrogenators:

$$v_i = \left\lceil \frac{\sum_{j=1}^{n_i} M_{hfcv,t}{}^{j} (\rho_2 + 1)}{P_2 k_{2,x}} \right\rceil \tag{16}$$

where ρ_1 is the charging margin of the EHCIS; P_1 is the rated power of each charging pile; $k_{1,x}$ is the charging efficiency of the charging pile; ρ_2 is the hydrogen injection margin of the hydrogen dispenser in the EHCIS; P_2 is the rated hydrogen injection capacity of a single hydrogen dispenser; $k_{2,x}$ is the hydrogen injection efficiency of the hydrogen dispenser; $q_{ev,t}{}^{j}$ denotes the demand for electric loads of EVs in the service area of the EHCIS i at time t; $M_{hfcv,t}{}^{j}$ denotes the demand for hydrogen of HFCVs in the service area of the EHCIS i at time t; and [] is the sign of upward rounding.

5.3. Constraints

EHCIS operational constraints include electrolyzer equipment constraints; hydrogen energy flow balance constraints; number of EHCIS constraints; distance between EHCIS constraints; and maximum distance from intersection constraints.:

(1) Electrolyzer Hydrogen Production Constraints:

The electrolyzer consumes electricity to produce hydrogen, which is commonly obtained using Equations (17)~(20) [7]:

$$P_{i,\text{elec}}^{t,d} = H_{\text{H}} \frac{F_{i,\text{elec}}^{t,d}}{\eta_{\text{elec}}} \tag{17}$$

$$w_i = \text{ceil}\left[\frac{\sum\limits_{j=1}^{n_i}\sum\limits_{t=1}^{24} P_{\text{elec},t}^{j}}{P_{\text{elec}}}\right] \tag{18}$$

$$0 \le F_{i,\text{elec}}^{t,d} \le \Gamma_{i,\text{elec}} \tag{19}$$

$$\underline{\Gamma_{i,\text{elec}}} \le \Gamma_{i,\text{elec}} \le \overline{\Gamma_{i,\text{elec}}} \tag{20}$$

where $P_{i,\text{elec}}^{t,d}$ is the input power of the electrolyzer at time t on day d of the year in EHCIS i; H_{H} is the high calorific value of hydrogen; $F_{i,\text{elec}}^{t,d}$ is the hydrogen productivity of the electrolyzer at time t on day d of the year in EHCIS i; η_{elec} is the energy conversion efficiency of the electrolyzer; $\Gamma_{i,\text{elec}}$ is the hydrogen production capacity of the electrolyzer in EHCIS i; and $\underline{\Gamma_{i,\text{elec}}}$ and $\overline{\Gamma_{i,\text{elec}}}$ denote the lower and upper limits of the hydrogen production rate of the electrolyzer in EHCIS i, respectively;

(2) Hydrogen Storage Tank Capacity Constraints:

The hydrogen produced in the electrolyzer is not immediately consumed by the fuel cell vehicle but is stored in a hydrogen storage tank. The hydrogen energy flow balance is calculated according to Equation (21) [7].

$$C_{i,\tan\text{k}}^{t+1,d} = C_{i,\tan\text{k}}^{t,d} - M_{i,\text{out}}^{t,d} + F_{i,\text{elec}}^{t,d} \tag{21}$$

where $C_{i,\tan\text{k}}^{t,d}$ and $C_{i,\tan\text{k}}^{t+1,d}$ are the hydrogen storage capacity in the hydrogen storage tank at time t and $t+1$ on day d, respectively; $M_{i,\text{out}}^{t,d}$ is the hydrogen storage capacity in the hydrogen storage tank at time t on day d; and $F_{i,\text{elec}}^{t,d}$ is the hydrogen inflow from the hydrogen dispenser to the hydrogen storage tank at time t on day d in the hydrogen storage tank in the EHCIS. The hydrogen storage tank constraints can be expressed as Equations (22) and (23) [34];

$$0 \le C_{i,\tan\text{k}}^{t,d} \le h_i \tag{22}$$

$$\underline{h_i} \le h_i \le \overline{h_i} \tag{23}$$

where h_i is the capacity of the hydrogen storage tank; $\underline{h_i}$ is the lower limit of the rated hydrogen storage capacity of hydrogen storage tank i of the electric hydrogen refueling station; $\overline{h_i}$ is the upper limit of the rated hydrogen storage capacity of hydrogen storage tank i of the EHCIS;

(3) Number of EHCIS constraints

$$N_{\min} \le N \le N_{\max} \tag{24}$$

where $N_{\min}$ and $N_{\max}$ are the minimum and maximum values of the number of EHCIS allowed to be built in the planning area.

(4) Distance Constraints Between EHCIS

$$D_{\min} \le D_{ij} \le D_{\max} \quad i \ne j \tag{25}$$

where D_{ij} is the straight-line distance between EHCIS i and EHCIS j; $D_{\min}$ and $D_{\max}$ are the minimum and maximum distances between EHCIS i and EHCIS j, respectively.

(5) Distance Constraints from Traffic Intersections to EHCIS

$$d_{ij} \le d_{\max} \tag{26}$$

where d_{ij} is the distance from the EHCIS to the traffic demand point; $d_{\max}$ is the maximum distance from the traffic demand point to the EHCIS; N_{cross} is the number of traffic intersections.

5.4. Improved Particle Swarm Optimization Algorithm

Because the EHCIS siting and capacity model contains variables such as charging piles, hydrogen refueling stations, the distance between the EHCIS, the demand point of automobile refueling, the charging equipment, and hydrogen refueling equipment in the EHCIS, which is difficult to be solved using the conventional mathematical methods, this paper adopts the improved particle swarm algorithm based on the division of the Voronoi diagram [35] for the model of the EHCIS.

5.4.1. Weighting Update Strategy

In this paper, the inertia weights in the traditional particle swarm algorithm are improved to solve the problems of easily falling into the local optimum at the beginning of the iteration and easily oscillating at the end of the iteration [36], and the inertia weights w are updated in each iteration. When the inertia weight is large, the particle has a strong ability in the global search, but at the same time, the adaptation update rate is slow; when the inertia weight w is small, the algorithm is strong in the local region search, but it is easy to fall into local optimal solutions. Therefore, this paper adopts the linear decreasing strategy [37,38] to update w, and the specific update formula is Equation (27) [39]:

$$w = w_{\max} - \frac{T \cdot (w_{\max} - w_{\min})}{T_{\max}} \tag{27}$$

where $w_{\max}$ and $w_{\min}$ are the maximum and minimum values of the inertia weights, respectively; and T and $T_{\max}$ are the current and maximum iterations, respectively.

5.4.2. Solution Process

The solution flow chart of the EHCIS is shown in Figure 4, which is mainly divided into the following seven steps:

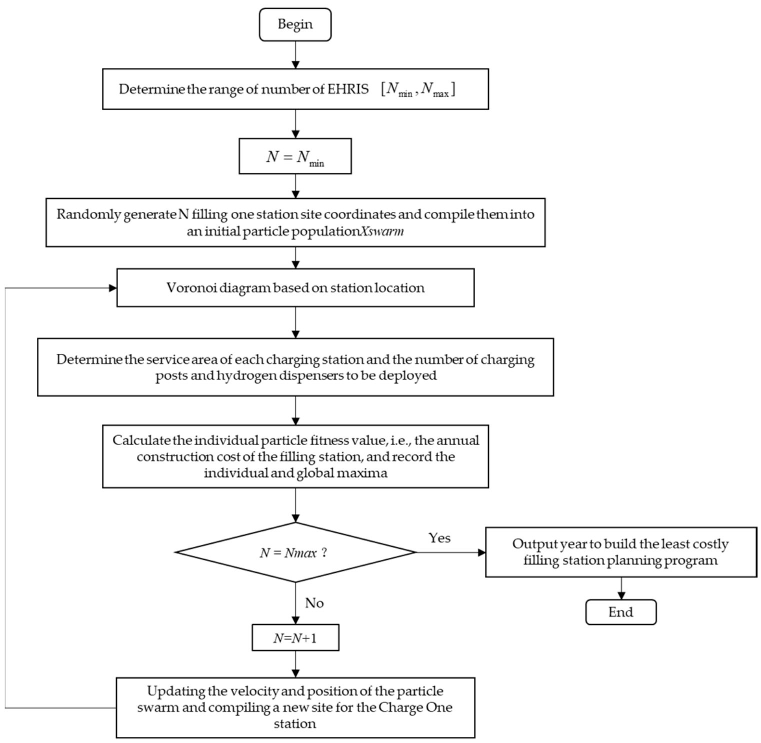

Figure 4. EHCIS solving flow chart.

Step 1: Calculate the electricity and hydrogen demand of urban transportation nodes based on the start and end of EV and HFCV trips in the planning area.

Step 2: Generate the coordinates of the site of the EHCIS and compile them into the initial location of the EHCIS.

Step 3: Make a Voronoi diagram with the initial site of the EHCIS as the growth point to determine the service area of each EHCIS and determine the number of charging piles and hydrogen dispensers according to the electricity and hydrogen load demand within the service area.

Step 4: Calculate the annual social cost of the EHCIS according to the objective function of planning, use it as the adaptation degree, and, finally, find the individual extreme value of the particle and the global extreme value.

Step 5: Judge whether the maximum number of iterations is reached. Yes, go to step 7; No, execute step 6.

Step 6: Update the velocity and position of the particle, jump to step 3, iteration number 1.

Step 7: Output the planning scheme that minimizes the objective function.

5.5. Grid Planning for Combined Electric Hydrogen Charging Station

In the case of EHCIS access, in order to ensure the safe and stable operation of the power grid, the active distribution network expansion planning is established, and the active distribution network management factors include [40] (1) an on-load voltage-regulating power transformer (on-load tap changer (OLTC)); (2) reactive power device regulation, including discrete reactive power compensation and continuous reactive power regulation; and (3) an energy storage system (ESS). In synthesizing the electric hydrogen production and EHCIS and management factors, this paper adopts the optimal current model of the distribution network from the literature using the following equation [41]:

$$\min f(p,q,P,Q,\widetilde{V},\widetilde{I})$$

$$s.t.\begin{cases} p_j=\sum_{k\in\delta(j)}P_{jk}-\sum_{i\in\pi(j)}(P_{ij}-\widetilde{I}_{ij}r_{ij})+g_j\widetilde{V}_j, & \forall j\in B \\ q_j=\sum_{k\in\delta(j)}Q_{jk}-\sum_{i\in\pi(j)}(Q_{ij}-\widetilde{I}_{ij}x_{ij})+b_j\widetilde{V}_j, & \forall j\in B \end{cases} \tag{28}$$

$$\widetilde{V}_j=\widetilde{V}_i-2(P_{ij}r_{ij}+Q_{ij}x_{ij})+\widetilde{I}_{ij}(r_{ij}^2+x_{ij}^2), \quad \forall ij\in E \tag{29}$$

$$\left\|\begin{matrix} 2P_{ij} \\ 2Q_{ij} \\ \widetilde{I}_{ij}-\widetilde{V}_j \end{matrix}\right\|_2 \le \widetilde{I}_{ij}+\widetilde{V}_j, \quad \forall ij\in E \tag{30}$$

$$\underline{I_{ij}^2}\le\widetilde{I}_{ij}\le\overline{I_{ij}^2}, \quad \forall ij\in E \tag{31}$$

$$\underline{V_j^2}\le\widetilde{V}_j\le\overline{V_j^2}, \quad \forall j\in B^+ \tag{32}$$

6. Active Management Element Modeling

6.1. OLTC Modeling

OLTC mainly regulates the HV/MV low-voltage side voltage value. With the addition of OLTC, the substation bus node is converted into an adjustable variable, which can be replaced as follows [42]:

$$\begin{cases} \underline{V_j^2}\le(V_{j,t}^{\text{Base}})^2 r_{j,t}\le\overline{V_j^2} \\ r_j^{\min}\le r_{j,t}\le r_j^{\max} \end{cases}, \forall t,\forall j\in B^{\text{OLTC}} \tag{33}$$

where B^{OLTC} is the set of substation nodes containing the OLTC; $V_{j,t}^{Base}$ is the voltage value of the high voltage side of the HV/MV transformer, which is constant; r_j^{max} and $r_j^{\min}$ are the squares of the upper and lower limits of the OLTC adjustable ratios; and $r_{j,t}$ is the square of the OLTC ratios, which is defined as the ratio of the secondary to the primary side and is actually a discrete-valued variable, which can be further processed into the following relationship containing 0–1 variables [42]:

$$r_{j,t} = r_j^{\min} + \sum_s r_{j,s} \sigma_{j,s,t}^{\text{OLTC}}, \quad \forall t, \forall j \in B^{\text{OLTC}} \tag{34}$$

where $r_{j,s}$ denotes the difference between the OLTC gear s and the square of the variable ratio of gear $s-1$, i.e., the neighboring regulation increment. $\sigma_{j,s,t}^{\text{OLTC}}$ is a 0–1 identifying variable, which can be expressed as Equation (35) if the constraints such as the limit on the number of regulation times are considered [43]:

$$\begin{cases} \sigma_{j,1,t}^{\text{oLTC}} \geq \sigma_{j,2,t}^{\text{oLTC}} \geq \sigma_{j,\text{SR}_j,t}^{\text{oLTC}},\ \forall t, \forall j \in B^{\text{OLTC}} \\ \delta_{j,t}^{\text{OLTC,IN}} + \delta_{j,t}^{\text{OLTC,DE}} \leq 1,\ \forall t, \forall j \in B^{\text{OLTC}} \\ \sum\limits_s \sigma_{j,s,t}^{\text{OLTC}} - \sum\limits_s \sigma_{j,s,t-1}^{\text{OLTC}} \geq \delta_{j,t}^{\text{OLTC,N}} - \delta_{j,t}^{\text{OLTC,DE}} \text{SR}_j, \\ \qquad \forall t, \forall j \in B^{\text{OLTC}} \\ \sum\limits_s \sigma_{j,s,t}^{\text{OLTC}} - \sum\limits_s \sigma_{j,s,t-1}^{\text{OLTC}} \leq \delta_{j,t}^{\text{OLTC,IN}} \text{SR}_j - \delta_{j,t}^{\text{OLTC,DE}}, \\ \qquad \forall t, \forall j \in B^{\text{OLTC}} \\ \sum\limits_{t \in T} (\delta_{j,t}^{\text{OLTC,IN}} + \delta_{j,t}^{\text{OLTC,DE}}) \leq N_j^{\text{OLTC,max}}, \forall j \in B^{\text{OLTC}} \end{cases} \tag{35}$$

where $\delta_{j,t}^{\text{OLTC,IN}}$ and $\delta_{j,t}^{\text{OLTC,DE}}$ indicate the OLTC gear adjustment change identification. For 0–1 variables, if $\delta_{j,t}^{\text{OLTC,IN}} = 1$, then the OLTC gear value in the t time period than the t-1 time period gear value is larger, the variable $\delta_{j,t}^{\text{OLTC,DE}}$ is similar. $\text{SR}_j^{\text{OLTC}}$ is the maximum change range of the gear and $N_j^{\text{OLTC,max}}$ is the maximum permissible number of adjustments of the OLTC gear in the T time period.

6.2. Modeling of Reactive Power Regulation Devices

(1) Discrete reactive power compensation modeling. Take the example of group switching capacitor banks (CB) [43].

$$\begin{cases} Q_{j,t}^{\text{CB}} = y_{j,t}^{\text{CB}} Q_j^{\text{CB,step}} \\ y_{j,t}^{\text{CB,max}} \leq Y_j^{\text{CB,max}} \end{cases}, \quad \forall t, \forall j \in B^{\text{CB}} \tag{36}$$

where B^{CB} is the set of CB nodes; $y_{j,t}^{\text{CB}}$ is the number of operating groups, which is the value of the discrete variable; $Y_j^{\text{CB,max}}$ is the upper limit of the number of CB groups connected to node j; $Q_j^{\text{CB,step}}$ is the compensated power of each group of CBs. Considering factors such as equipment life or economy, discrete reactive power compensation is mostly limited by the number of adjustments, so it generally includes a limit on the total number of operations in multiple time periods; and $N_j^{\text{CB,max}}$ is the upper limit of the number of operations [44]:

$$\sum_{t \in T} \left| y_{j,t}^{\text{CB}} - y_{j,t-1}^{\text{CB}} \right| \leq N_j^{\text{CB,max}}, \quad \forall t, \forall j \in B^{\text{CB}} \tag{37}$$

Then it is available:

$$\delta_{j,t}^{\text{CB}} = \left| y_{j,t}^{\text{CB}} - y_{j,t-1}^{\text{CB}} \right| \tag{38}$$

$$\begin{cases} \sum_{t \in T} \delta_{j,t}^{\text{CB}} \leq N_j^{\text{CB,max}} \\ -\delta_{j,t}^{\text{CB,max}} \leq y_{j,t}^{\text{CB}} \leq \delta_{j,t}^{\text{CB,max}} Y_j^{\text{CB,max}} \end{cases}, \quad \forall t, \forall j \in B^{\text{CB}} \tag{39}$$

(2) Modeling of continuous reactive power regulation devices. Take a static VAR compensation (SVC) device as an example. Continuous reactive power regulation is relatively simple compared to discrete reactive power compensation devices [45].

$$Q_j^{\mathrm{SVC,min}} \le Q_{j,t}^{\mathrm{SVC}} \le Q_j^{\mathrm{SVC,max}}, \quad \forall t, \forall j \in B^{\mathrm{SVC}} \tag{40}$$

where B^{SVC} is the set of nodes containing SVC and $Q_j^{\mathrm{SVC,min}}$ and $Q_j^{\mathrm{SVC,max}}$ are the lower and upper limits of the SVC compensation power, respectively. The increasing penetration of DGs such as PV power generation, may cause system current reversal and over-voltage problems, so the lower limit of SVC compensation in this paper $Q_j^{\mathrm{SVC,min}} < 0$.

6.3. Modeling of Energy Storage Systems

Typically, the energy storage system (ESS) needs to consider the constraint limitations of multiple time periods, which mainly contain the charging and discharging state limitations, the charging and discharging power limitations, and the energy storage capacity constraints.

(1) The charge and discharge state constraint is expressed in Equation (41) [46]:

$$u_{j,t}^{\mathrm{discharge}} + u_{j,t}^{\mathrm{charge}} \le 1, \quad \forall j \in B^{\mathrm{ESS}}, \forall t \tag{41}$$

(2) The power constraint is expressed in Equation (42) [47]:

$$\begin{cases} u_{j,t}^{\mathrm{discharge}} P_j^{\mathrm{discharge,min}} \le P_{j,t}^{\mathrm{discharge}} \le u_{j,t}^{\mathrm{discharge}} P_j^{\mathrm{discharge,max}} \\ u_{j,t}^{\mathrm{charge}} P_j^{\mathrm{charge,min}} \le P_{j,t}^{\mathrm{charge}} \le u_{j,t}^{\mathrm{charge}} P_j^{\mathrm{charge,max}}, \forall t, \forall j \in B^{\mathrm{ESS}} \end{cases} \tag{42}$$

(3) The capacity constraint is expressed in Equation (43) [48]:

$$\begin{cases} E_{j,t+1}^{\mathrm{ESS}} = E_{j,t}^{\mathrm{ESS}} + \alpha_j^{\mathrm{charge}} P_{j,t}^{\mathrm{charge}} - \alpha_j^{\mathrm{discharge}} P_{j,t}^{\mathrm{discharge}} \\ E_j^{\mathrm{ESS,min}} \le E_{j,t}^{\mathrm{ESS}} \le E_j^{\mathrm{ESS,max}}, \forall j \in B^{\mathrm{ESS}}, \forall t \end{cases} \tag{43}$$

where B^{ESS} is the set of nodes containing ESS. Equation (43) indicates that ESS cannot be charged and discharged at the same time; $u_{j,t}^{\mathrm{charge}}$ and $u_{j,t}^{\mathrm{discharge}}$ are the ESS charging and discharging states; $P_j^{\mathrm{discharge,max}}$, $P_j^{\mathrm{charge,max}}$, $P_j^{\mathrm{charge,min}}$, and $P_j^{\mathrm{discharge,min}}$ are the upper and lower limits of the ESS charging and discharging power, respectively; $E_{j,t}^{\mathrm{ESS}}$ is the ESS power in the t time period, $E_j^{\mathrm{ESS,max}}$ and $E_j^{\mathrm{ESS,min}}$ are the upper and lower limits of the ESS taking into account the ESS lifetime, etc.; and $\alpha_j^{\mathrm{charge}}$ and $\alpha_j^{\mathrm{discharge}}$ are the charging and discharging efficiency coefficients, in general, $\alpha_j^{\mathrm{charge}} < 1$ and $\alpha_j^{\mathrm{discharge}} > 1$.

Based on the comprehensive consideration of the active management element modeling, the coordination planning of the EHCIS with the distribution grid is carried out based on the geographic characteristics of the planning area of the EHCIS.

7. Algorithm Analysis

7.1. Electricity-Hydrogen Demand Calculations

In this paper, 24 nodes in Sioux Falls are selected to describe the urban road network structure. The specific network topology is shown in Figure 5. The road network structure for automobile travel includes 24 nodes and 38 roads. The starting point of the car is set to have 2000 EVs and 1000 HFCVs in the transportation network, the rated capacity of the EV is set to 60 kWh, the capacity of the HFCV is 4 kg, and the time-sharing tariff is shown in the Appendix A Table A1 [49]. Where $a_1 = 80,000$ ￥, $a_2 = 400,000$ ￥, $b_1 = 150,000$ ￥, $b_2 = 300,000$ ￥, $c_2 = 9261$ ￥/kg, $d_2 = 22,000$ ￥, $c_i = 180,000$ ￥, $z = 20$, $r_0 = 0.8\%$,

$\eta = 0.05$, $\eta_{\text{elec}} = 0.73$, $h_0 = 54$ ¥/kg, $g_{ev} = 0.16\,\text{kWh/km}$, $g_{hev} = 0.118\,\text{kg/km}$, $\rho_1 = \rho_2 = 0.1$, $P_1 = 48\,\text{kW/h}$, $P_2 = 700\,\text{kg/day}$, $P_{elec} = 39\,\text{kWh/kg}$, and $H_{\text{H}} = 3.509\,\text{kW} \cdot \text{h/m}^3$. Monte Carlo sampling was used to calculate the spatial and temporal distribution of electric energy demand and hydrogen energy demand in the transportation network by searching for the path with the minimum travel time through Dijkstra's algorithm based on the OD matrices of EVS and HFCVs, as shown in Figures 6 and 7.

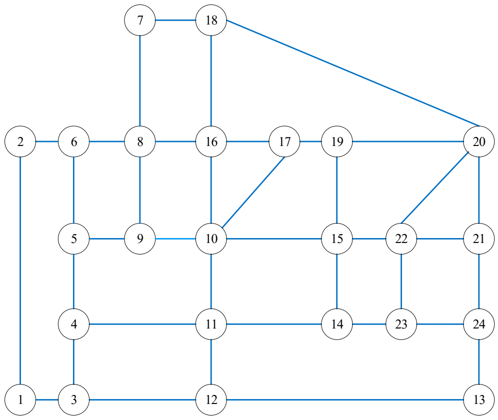

Figure 5. Sioux Falls network topology diagram.

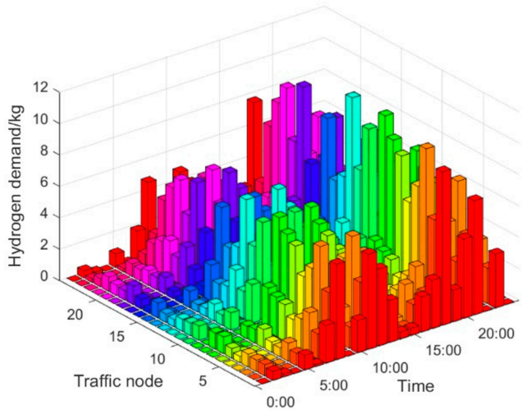

Figure 6. Hydrogen load demand distribution in transportation.

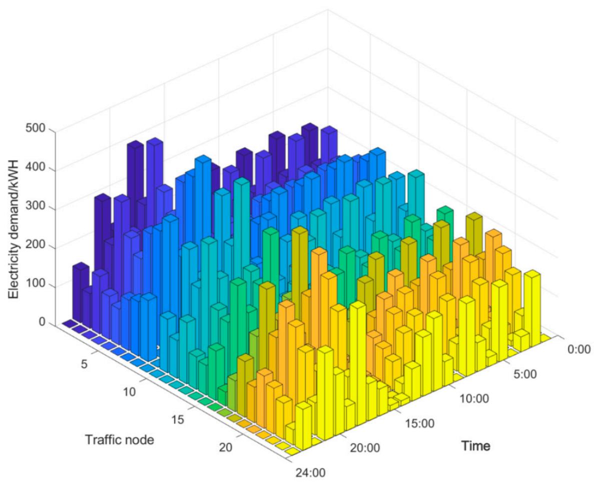

Figure 7. Electric load demand distribution in traffic.

As can be seen from Figure 6, the main time distribution of hydrogen demand for HFCVs peaks at 12:00–13:00 and 21:00–23:00, mainly due to the fact that HFCV users focus on hydrogen injection at the time of returning from noon and returning from work. HFCVs have a short hydrogen injection time, which is negligible compared to the charging time of EVs, and the number of HFCVs is small compared to the number of EVs in practice. The construction cost of the charging equipment for EVs is less, and the construction cost of hydrogen injection equipment for HFCVs is high, and there are many hydrogen production links. Figure 7 shows that the charging behavior of EVs is more random, and the electric load distribution of EVs is more intensive compared to the hydrogen load demand of HFCVs.

7.2. Simulation Results

Based on the loads of EVs and HFCVs, the EHCIS in Sioux Falls are selected for capacity planning. Set the number of particle population species as 20, $T_{\max}$ is set to be 300 and the number of EHCIS in the planning area is set as 3~20, and this number of EHCIS is solved by traversing. The simulation results are shown in Figure 8 and Table 2, and the two algorithms are iterated as the iteration process in Figure 9.

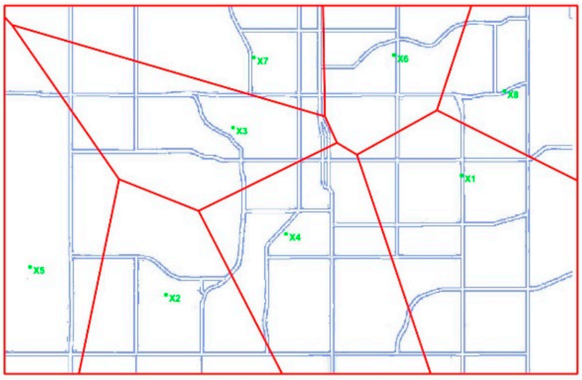

Figure 8. Schematic diagram of planning results.

Table 2. Comprehensive annual economic construction cost of EHCIS.

Quantities	C_1 ($\times10^6$ ¥)	C_2 ($\times10^6$ ¥)	C_3 ($\times10^6$ ¥)	C_4 ($\times10^6$ ¥)	C ($\times10^6$ ¥)
7	5063.76	253.19	39.7	42.83	5379.48
8	5083.92	254.19	38.38	22.08	5398.57
9	5115.72	255.78	38.18	22.34	5432.02
10	5153.09	257.65	37.43	21.8	5469.97

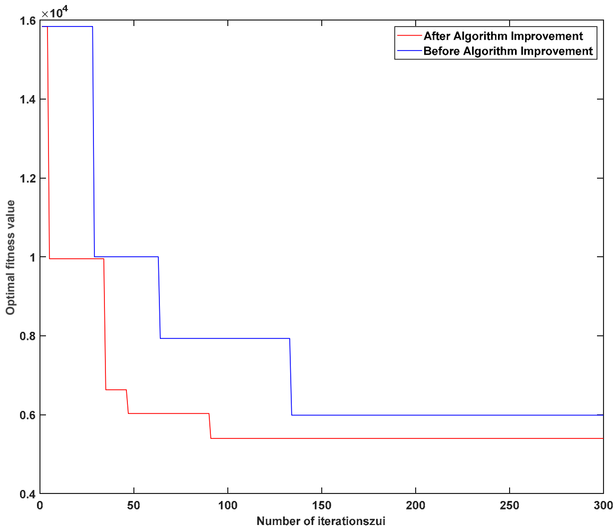

Figure 9. Iterative process.

When the number of EHCIS sites is 7~10, the corresponding annual total social cost of EHCIS construction is shown in Table 3. The optimal solution C appears when the number of EHCIS is 8. Each EHCIS contains charging piles, electrolyzers, hydrogen storage tanks, and hydrogen dispensers, and the number of charging piles and electrolyzers in the EHCIS is solved by Equations (15) and (16); Equations (15) and (16) both adopt the method of rounding upwards by [], which means that the utilization rate of the charging piles and electrolyzers in the EHCIS cannot reach 100% and the construction cost increases with the increase of the number of EHCIS sites. The fixed construction cost of EHCIS also increases with the number of EHCIS sites. The maintenance cost C_2 of EHCIS is solved by Equation (12), and the fixed construction C_1 and maintenance cost C_2 increase by 1.76% as the cost C_1 increases from 5063.76×10^6 ¥ to 5153.09×10^6 ¥ and the maintenance cost C_2 increases from 253.19×10^6 ¥ to 257.65×10^6 ¥. When the number of EHCIS increases, the utilization rate of the charging piles and electrolyzers in the EHCIS increases, and the cost of the charging piles for charging and the electricity consumption for hydrogen production gradually decrease. Since the number of electric vehicles and hydrogen fuel cell vehicles in the planning area remains constant, the demand for electricity and hydrogen remains essentially the same, so the costs C_3 remain essentially the same, and C_3 decreases by −6.07% as the EHCIS changes from site 7 to 10. Due to the increase in the number of EHCIS sites, although the cost of the EHCIS equipment increases, the distance from the electric vehicles and hydrogen fuel cell vehicles to each EHCIS becomes smaller, so the cost of C_4 decreases from 42.83×10^6 ¥ to 21.8×10^6 ¥, making the total cost C show a decreasing and then increasing trend.

Table 3. Configuration parameters of each EHCIS.

EHCIS Number	Number of Charging Piles	Number of Electrolytic Tanks	Hydrogen Storage Tank Capacity/(kg)	Number of Hydrogen Injectors
X1	17	97	7.9	1
X2	10	96	7.6	1
X3	13	136	11.2	1
X4	23	298	20.1	1
X5	2	19	1.46	1
X6	14	132	10.1	1
X7	27	199	19.4	1
X8	1	7	0.54	1

The eight EHCIS are numbered from X1 to X8, the optimal locations of the EHCIS are shown in Figure 7, and the configurations of the charging piles, electrolysis tanks, hydrogen storage tanks, and hydrogen dispensers of each EHCIS are shown in Table 3. HFCVs account for a low proportion in the transportation field, the number is small, and the hydrogen filling capacity of the hydrogen dispenser is large. One hydrogen dispenser can reach 700 kg of hydrogen per day [50]; therefore, only one EHCIS can meet the demand for hydrogen filling in the planning area of the city.

Discuss the time complexity and space complexity of the particle swarm algorithm given that the number of particles is 20, the number of EHCIS sites is 8, and the number of iterations is 300:

(1) Time complexity:

The time complexity of the particle swarm algorithm is mainly related to the number of iterations, the computational operations in each iteration, and the dimension of the problem. Let the computation in each iteration be O (V), where V denotes the dimension of the problem. The overall time complexity is O ($T \times V \times N$), where T is the number of iterations and N is the number of particles. In this case, the overall time complexity is O (300 * 16 * 20) = O (9600).

(2) Space complexity:

Each particle needs to store information, such as the position (16 variables), velocity (16 variables), and fitness value. Therefore, the storage space complexity of each particle is O (V), where V is the dimension of the problem. The overall space complexity is O ($N \times V$), where N is the number of particles. In this case, the total space complexity is O (20 * 16) = O (320).

7.3. Integrated Distribution Network Planning

The modified IEEE33 node system is used for the analysis, and the network parameters are detailed in the literature [51]. In this paper, OLTC, ESS, CB, SVC, wind turbines, and electric EHCIS are added to the basic network to realize the collaborative planning of the EHCIS and the distribution network. The modification is shown in Figure 10. In this case, an OLTC is connected between nodes 33 and 1; node 5, node 15, and node 31 are connected to SVC; node 5 and node 15 are connected to CB; nodes 15 and 32 are connected to ESS; and nodes 17 and 32 are connected to the wind farm, respectively. The EHCIS are connected to nodes 19, 3, 7, 23, 13, 27, 10, and 14, respectively. The wind power and load data in the example are from the actual system. The OLTC ratio range is assumed to be, and the active management equipment parameters are detailed in Appendix A Tables A2–A4. The literature [19] has demonstrated that the relaxation model with grid losses as the objective function is rigorously accurate, and, in addition to this, the objective function of this planning includes the sum of the power purchases from the higher grid. The program is computed in a Matlab R2018a environment based on CPLEX 12.8.0 with an i5-12400 CPU 2.5 GHz, 16 GB RAM (Intel, Santa Clara, CA, USA), and a Win10 64-bit operating system.

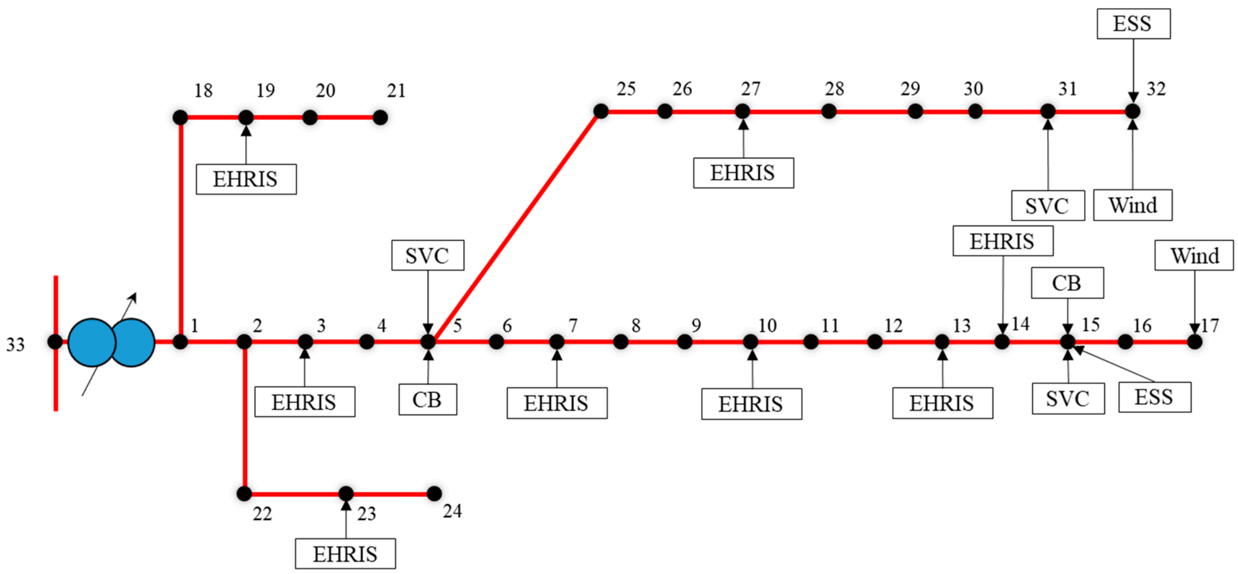

Figure 10. Modified IEEE33 nodes.

According to the original data of the arithmetic example, the active coordination optimization yields the results of each equipment for each time period, as shown in Figures 11–15. Figure 11 shows the 24-h distribution of the voltage at the IEEE33 node, Figure 12 shows the active output of the wind power, and Figures 13 and 14 show the output of the reactive power compensator capacitor bank CB and the reactive power compensator SVC, respectively.

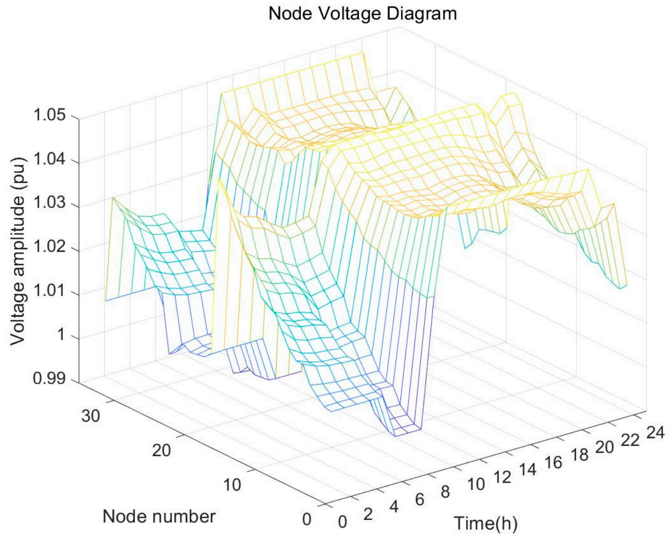

Figure 11. Voltage distribution.

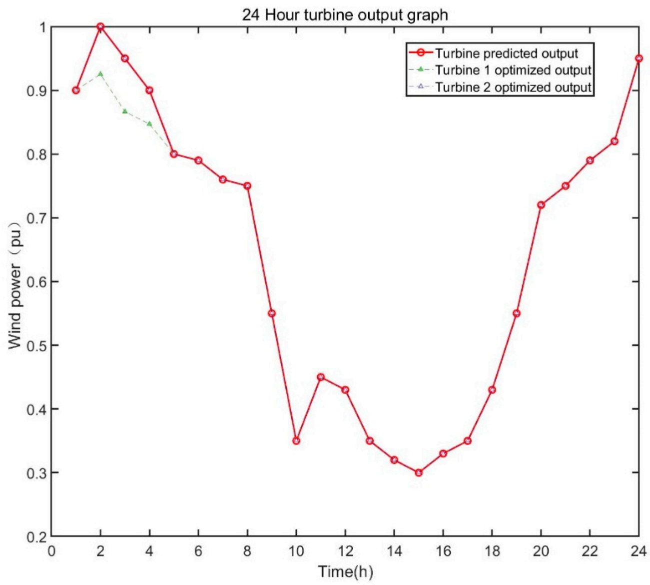

Figure 12. Actual 24-h turbine output.

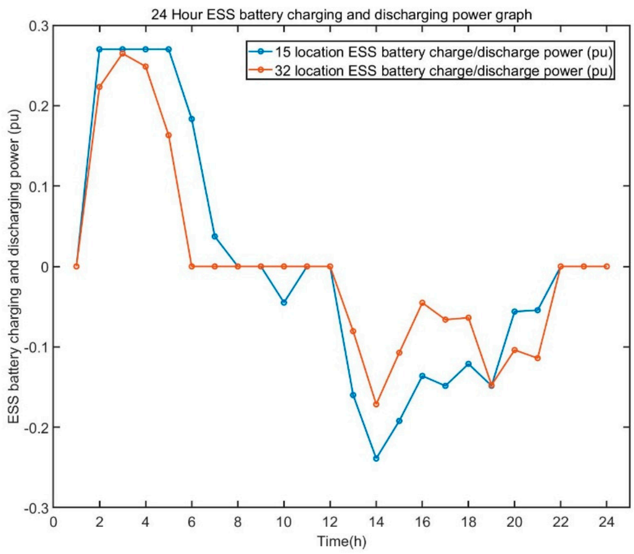

Figure 13. ESS charging and discharging power diagram.

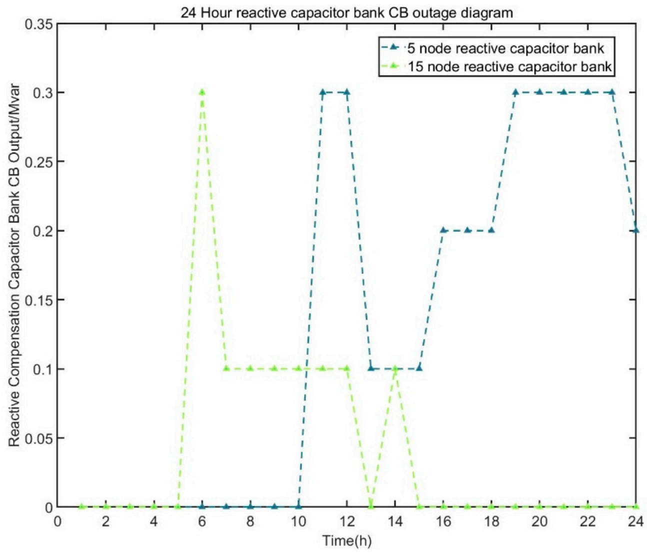

Figure 14. Output diagram of reactive power compensation capacitor bank CB.

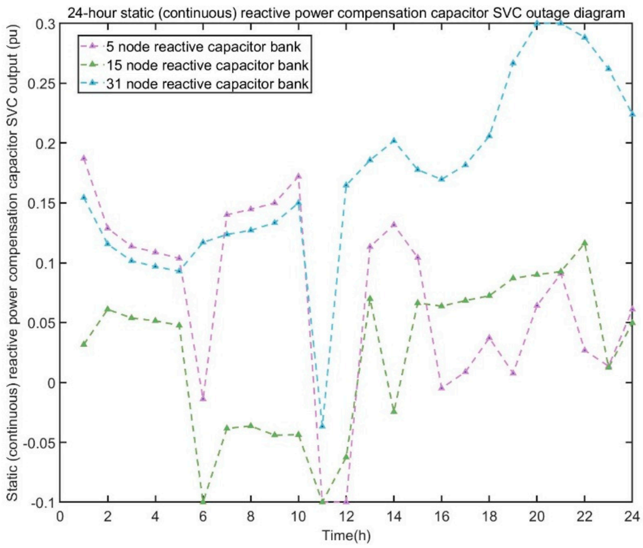

Figure 15. SVC output diagram of reactive power compensator.

From Figures 12–16, it can be seen that (1) in the load trough section (00:00–04:00), due to the need to ensure the lower value of 0.5 MW output of the main grid, the high wind turbine output at night, and the storage of new energy sources in the night, the ESS is limited by the capacity, and it cannot further absorb the excess clean energy, which leads to power abandonment, and ESS discharges at the peak load stage, effectively reduces the equivalent load peak–valley difference; at 6:00, the wind power output gradually decreases, the ESS charging power becomes smaller, and in the daytime, as electric vehicles and hydrogen fuel cell vehicles begin to run, the power consumed by the EHCIS, as an active load, begins to increase. it can be concluded from Figure 11 that the voltage begins to rise in the time period from 4:00 to 6:00, accompanied by an increase in active loads, and, in order to maintain voltage stability in the distribution network, the reactive power compensation power supply is required to maintain the voltage stability in the distribution network, and the ESS is not able to further absorb the excess clean energy. In order to maintain the voltage stability in the distribution network, the output of both THE reactive power compensation capacitor bank CB and the reactive power compensator SVC start to increase gradually to avoid the appearance of nodal overvoltage in the distribution network.

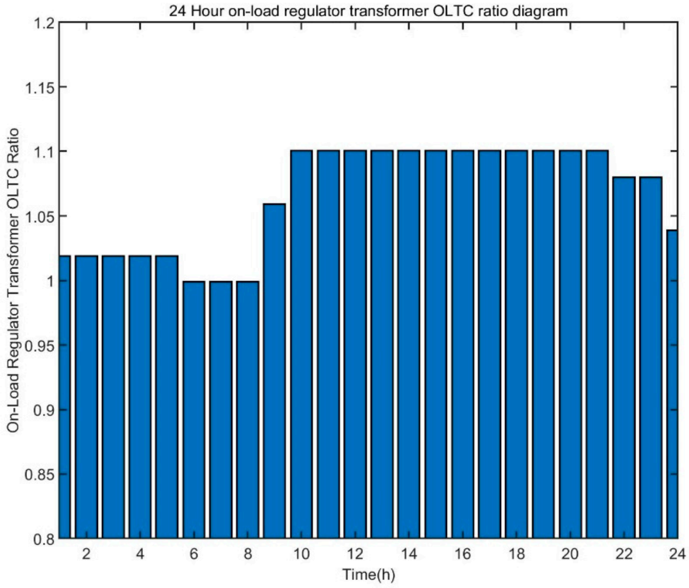

Figure 16. OLTC ratio diagram for on-load regulator transformer.

During the time when the wind power output is higher (nighttime), with an increase in electricity consumption, the OLTC increases the voltage, and the reactive device absorbs the excess reactive power of the system in this time period. The peak period of electricity consumption of automobile users commuting to and from work and residential users is 18:00~24:00, and the wind turbine output is gradually increased in this time period. In addition, due to the gradual increase in the electricity load, the ESS storage device begins to discharge, and in the node of the distribution grid, there is a boosting trend in the nighttime time period, but along with the increase in the output of the reactive power compensation capacitor bank CB and the reactive power compensator SVC, the distribution network node voltage is still kept within the $\pm$5% deviation.

8. Conclusions

The large-scale promotion of new energy vehicles requires the infrastructure of EHCIS as a prerequisite, and the large-scale integration of new energy vehicles into the grid will have an impact on the power grid. Therefore, in order to meet the demand for hydrogen energy for automobiles, it is necessary to consider the coordinated planning of the EHCIS and the power distribution network. In this paper, the model of EHCIS is designed to minimize the total social cost in the planning area, and the particle swarm method is used to solve the model for the highly nonlinear characteristics of the model, which contains many variables. The Voronoi diagram of the EHCIS site is the growth point, and the area formed by the growth is the service area of the EHCIS. The equipment capacity of the EHCIS is determined according to the electric hydrogen demand of EVs and HFCVs in the service area, and the particle swarm algorithm is used to search for the optimal solution of the objective function of the planning of the EHCIS. The calculation results show the following:

(1) In this paper, the OD matrix and BPR road resistance function are used to simulate the travel trajectories of EVs and HFCVs, and the electric hydrogen demand of EVs and HFCVs is obtained by dynamically updating the state parameters of EVs and HFCVs in real time. The calculation results show that there is an obvious difference in the spatial and temporal distribution of the electric loads and hydrogen loads of EVs and HFCVs.

(2) This paper establishes an active management model on the basis of planning the EHCIS and verifies through example simulation that it meets the energy demand of EVs and HFCVs while ensuring the safe and reliable operation of the power grid and realizes the coordinated planning of the EHCIS and the power distribution grid. In this paper, the

spatial and temporal distribution of automobile energy demand is obtained by superimposing the demand of a single quantity of automobiles, and the planning of the EHCIS is carried out on the basis of obtaining the electric hydrogen energy demand of automobiles. Finally, by introducing reactive power compensation components and energy storage devices, the grid node voltage is maintained within a ±5% deviation during peaks and valleys, which ensures the safe and reliable operation of the system.

(3) The EHCIS holds distinct advantages over standalone charging stations [52]: the EHCIS combines electric and hydrogen refueling facilities, offering a dual-fuel solution for diverse vehicle types. This integrated approach optimizes spatial utilization, streamlines infrastructure development, and provides a comprehensive solution for both electric and hydrogen-powered vehicles. Additionally, the EHCIS minimizes the need for duplicate infrastructure, thereby reducing the overall land requirements and promoting a more efficient and sustainable energy transition for multi-modal transportation systems.

(4) In contrast to the insights from [53], our study stands out by emphasizing the integration of EHCIS into active distribution network planning. This strategic inclusion ensures the secure and reliable operation of the power grid, addressing the crucial aspect of grid connectivity. This paper not only introduces an innovative approach for the siting and capacity determination of EHCIS, utilizing Voronoi diagrams and particle swarm algorithms to calculate vehicle charging and hydrogen refueling demands but also underscores the significance of seamlessly incorporating EHCIS into existing energy infrastructures. This holistic perspective guarantees the safety and reliability of the power grid during the operation of these integrated stations, marking a substantial advancement in the field.

(5) PSO is a heuristic algorithm based on group collaboration, but it is not guaranteed to find a globally optimal solution. In the EHCIS siting and capacity determination problem, there are complex nonlinear relationships and constraints, which may cause PSO to fall into local optimality during the search process. In this paper, the initialization location of EHCIS is used as the optimization strategy after determining the location of EHCIS; therefore, Cplex is needed to deal with the hydrogen flow balance constraints, grid balance constraints, and so on. The siting and capacitation problem may involve multiple decision variables; when the dimension of the problem is high, the particle swarm algorithm may face a dimensional disaster, i.e., the performance of the algorithm decreases with an increase in the dimension of the problem. The search space of the PSO algorithm for the high-dimension problem may become too large, resulting in a decrease in the search efficiency.

Author Contributions: Project administration, X.T.; methodology, writing—review and editing, H.Y.; supervision, Y.G.; formal analysis and resources, T.Y. All authors have read and agreed to the published version of the manuscript.

Funding: This work is funded by the Science and Technology Project of State Grid Corporation of China (No.5400-202228170A-1-1-ZN).

Data Availability Statement: Vehicle data were derived from Monte Carlo simulations, urban road data were taken from the website from http://jlitraffic.appspot.com/tap.html and grid data from https://github.com/MATPOWER/matpower/tree/master/data.

Conflicts of Interest: Author Xueqing Tian was employed by the company China Electric Power Research Institute Co., Ltd. Author Yangyang Ge was employed by the company Electric Power Research Institute of State Grid Liaoning Electric Power Co., Ltd. The remaining authors declare that the research was conducted in the absence of any commercial or financial relationships that could be construed as a potential conflict of interest.

Appendix A

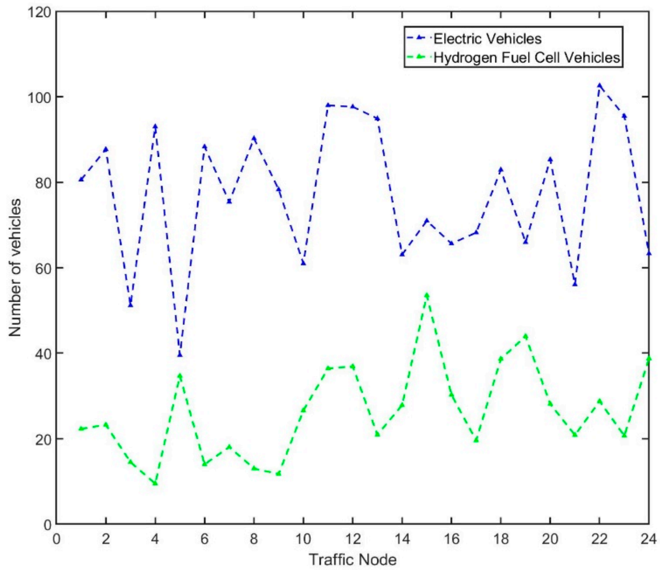

Figure A1. Number of starting cars at each traffic node.

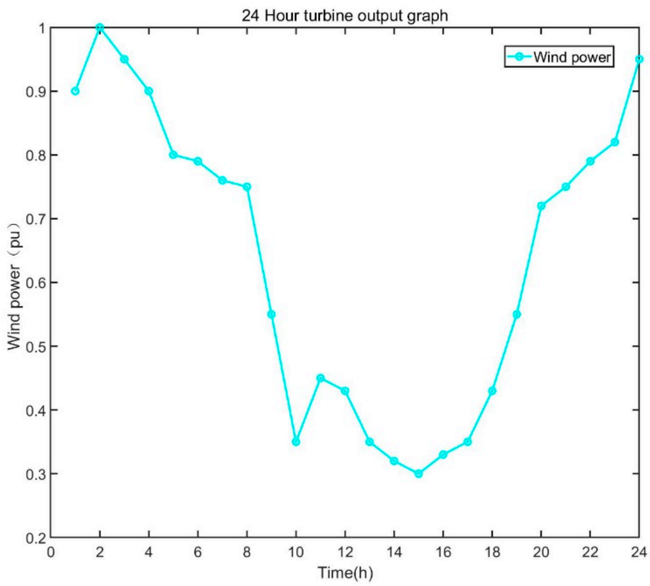

Figure A2. Wind turbine power curve.

Table A1. Tariffs for different time periods.

	Peak Period	Level Period	Valley Period
Time	(12:00–15:00) (20:00–23:00)	(9:00–12:00) (15:00–20:00) (23:00–0:00)	(0:00–9:00)
price of electricity (¥/kWh)	0.56	0.39	0.30

Table A2. Parameters of CB.

Nodes	Unit Capacity/Mvar	Quantities
5, 31	0.01	5

Table A3. Parameters of ESS.

Nodes	Limit of Power/MW	Limit of Capacity/(MW·h)	Charging Efficiency	Discharging Efficiency
15, 32	0.3	1.5	0.9	1.11

Table A4. Parameters of SVC.

Nodes	Compensation Coverage
5, 15, 31	[−0.1, 0.3]

References

1. Mahmud, N.; Zahedi, A.J.R.; Reviews, S.E. Review of control strategies for voltage regulation of the smart distribution network with high penetration of renewable distributed generation. *Renew. Sustain. Energy Rev.* **2016**, *64*, 582–595. [CrossRef]
2. Manoharan, Y.; Hosseini, S.E.; Butler, B.; Alzhahrani, H.; Senior, B.T.F.; Ashuri, T.; Krohn, J. Hydrogen fuel cell vehicles; Current status and future prospect. *Appl. Sci.* **2019**, *9*, 2296. [CrossRef]
3. Xu, H.; Miao, S.; Zhang, C.; Shi, D. Optimal placement of charging infrastructures for large-scale integration of pure electric vehicles into grid. *Int. J. Electr. Power Energy Syst.* **2013**, *53*, 159–165. [CrossRef]
4. Su, S. Method of Location and Capacity Determination of Intelligent Charging Pile Based on Recurrent Neural Network. *World Electr. Veh. J.* **2022**, *13*, 186. [CrossRef]
5. Awasthi, A.; Venkitusamy, K.; Padmanaban, S.; Selvamuthukumaran, R.; Blaabjerg, F.; Singh, A.K. Optimal planning of electric vehicle charging station at the distribution system using hybrid optimization algorithm. *Energy* **2017**, *133*, 70–78. [CrossRef]
6. Yang, G.; Jiang, Y.; You, S. Planning and operation of a hydrogen supply chain network based on the off-grid wind-hydrogen coupling system. *Int. J. Hydrogen Energy* **2020**, *45*, 20721–20739. [CrossRef]
7. Sun, H.; He, C.; Wang, H.; Zhang, Y.; Lv, S.; Xu, Y. Hydrogen station siting optimization based on multi-source hydrogen supply and life cycle cost. *Int. J. Hydrogen Energy* **2017**, *42*, 23952–23965. [CrossRef]
8. Kuby, M.; Lines, L.; Schultz, R.; Xie, Z.; Kim, J.-G.; Lim, S. Optimization of hydrogen stations in Florida using the flow-refueling location model. *Int. J. Hydrogen Energy* **2009**, *34*, 6045–6064. [CrossRef]
9. Gu, J.; Wang, C.; Xie, D. Research on optimal operation of electricity-hydrogen integrated station in electricity market environment. *J. Electr. Power Sci. Technol.* **2022**, *37*, 130–139.
10. Gao, C.; Wang, W.; Chen, T. Capacity Planning of Electric-hydrogen Integrated Energy Station Based on Reversible Solid Oxide Battery. *Proc. Chin. Soc. Electr. Eng.* **2022**, *42*, 6155–6169. [CrossRef]
11. LeBlanc, L.J.; Morlok, E.K.; Pierskalla, W.P. An efficient approach to solving the road network equilibrium traffic assignment problem. *Transp. Res.* **1975**, *9*, 309–318. [CrossRef]
12. Cervero, D.; Fotopoulou, M.; Muñoz-Cruzado, J.; Rakopoulos, D.; Stergiopoulos, F.; Nikolopoulos, N.; Voutetakis, S.; Sanz, J.F. Solid State Transformers: A Critical Review of Projects with Relevant Prototypes and Demonstrators. *Electronics* **2023**, *12*, 931. [CrossRef]
13. Alba, J.M.-C.; Fuertes, J.B.; Gomez, A.M.M.; Osorio, J.F.S.; Puyal, E.L. 50-kW Modular V2G SiC Charger Station in Energy Island Microgrids: A Real Use-Case in Madeira Island. In Proceedings of the PCIM Europe 2022; International Exhibition and Conference for Power Electronics, Intelligent Motion, Renewable Energy and Energy Management, Nuremberg, Germany, 10–12 May 2022; pp. 1–9.
14. Biya, T.S.; Sindhu, M.R. Design and Power Management of Solar Powered Electric Vehicle Charging Station with Energy Storage System. In Proceedings of the 2019 3rd International Conference on Electronics, Communication and Aerospace Technology (ICECA), Coimbatore, India, 12–14 June 2019; pp. 815–820.
15. Chen, M.; Lu, H.; Chang, X.; Liao, H. An optimization on an integrated energy system of combined heat and power, carbon capture system and power to gas by considering flexible load. *Energy* **2023**, *273*, 127203. [CrossRef]
16. Xue, P.; Zhao, B.; Zhang, L.; Deng, M.; Liu, J.; Huang, Y.; He, Z. Planning Method for Electric Vehicle Charging Station Considering Reliability Constraint. In Proceedings of the 2023 Panda Forum on Power and Energy (PandaFPE), Chengdu, China, 27–30 April 2023; pp. 1557–1561.
17. Chen, Z.; Chen, Y.; Che, S. Framework of Integrated Charging Station for Renewable Energy Vehicle and Energy Optimal Dispatching Method. *Autom. Electr. Power Syst.* **2019**, *43*, 41–49. [CrossRef]
18. Chen, L.; Yang, F.; Xing, Q.; Wu, S.; Wang, R.; Chen, J. Spatial-temporal distribution prediction of charging load for electric vehicles based on dynamic traffic information. In Proceedings of the 4th IEEE Conference on Energy Internet and Energy System Integration, EI2 2020, Wuhan, China, 30 October–1 November 2020; pp. 1269–1274.
19. Abdelouadoud, S.Y.; Girard, R.; Neirac, F.-P.; Guiot, T. Optimal power flow of a distribution system based on increasingly tight cutting planes added to a second order cone relaxation. *Int. J. Electr. Power Energy Syst.* **2015**, *69*, 9–17. [CrossRef]
20. Yuan, T.; Ji, L.; Tian, X.; Li, G. Synergistic Optimal Operation of Electricity-Hydrogen Systems Considering Hydrogen Refueling Loads for Fuel Cell Vehicles. *Autom. Electr. Power Syst.* **2023**, *47*, 16–25. [CrossRef]

21. Chen, L.; Zhang, Y.; Figueiredo, A. Charging load forecasting of electric vehicles based on multi-source information fusion and its influence on distribution network. *Electr. Power Autom. Equip.* **2018**, *38*, 1–10. [CrossRef]
22. Iliopoulou, C.; Kampitakis, E.; Kepaptsoglou, K.; Vlahogianni, E.I. Dynamic traffic-aware auction-based signal control under vehicle to infrastructure communication. *Phys. A Stat. Mech. Its Appl.* **2022**, *608*, 128258. [CrossRef]
23. Zhang, X.; Wang, Z.; Qian, W.; Hu, K.; Zhou, X.; Li, X. Spatio-temporal dynamic load forecasting of charging pile based on spatio-temporal neural network. *Shaanxi Electr. Power* **2019**, *47*, 50–54.
24. Zheng, Y.; Feng, L.I.; Dong, J. Optimal dispatch strategy of spatio-temporal flexibility for electric vehicle charging and discharging in vehicle-road-grid mode. *Autom. Electr. Power Syst.* **2022**, *46*, 88–97.
25. Zhang, L.; Xu, C.; Wang, L.; Li, J.; Chen, X.; Yang, X.; Shi, Y. OD matrix based spatiotemporal distribution of EV charging load prediction. *Power Syst. Prot. Control* **2021**, *49*, 82–91. [CrossRef]
26. Zu, S.; Sun, L. Research on location planning of urban charging stations and battery-swapping stations for electric vehicles. *Energy Rep.* **2022**, *8*, 508–522. [CrossRef]
27. Huang, C.-Y.; Lai, C.-Y.; Cheng, K.-T. CHAPTER 4—Fundamentals of algorithms. In *Electronic Design Automation*; Wang, L.-T., Chang, Y.-W., Cheng, K.-T., Eds.; Morgan Kaufmann: Boston, MA, USA, 2009; pp. 173–234.
28. Yen, J.Y. An algorithm for finding shortest routes from all source nodes to a given destination in general networks. *Q. Appl. Math.* **1970**, *27*, 526–530. [CrossRef]
29. Yu, T.; Ma, J. A review of the link traffic time estimation of urban traffic. In Proceedings of the 2016 IEEE International Conference on Intelligent Transportation Engineering, ICITE 2016, Singapore, 20–22 August 2016; pp. 123–127.
30. Shao, C.; Li, X.; Qian, T.; Wang, X.; Wang, X. Simulation of EV Fast Charging Load Based on Traffic Equilibrium. *Proc. Chin. Soc. Electr. Eng.* **2021**, *41*, 1368–1376. [CrossRef]
31. Othman, A.M.; Gabbar, H.A.; Pino, F.; Repetto, M. Optimal electrical fast charging stations by enhanced descent gradient and Voronoi diagram. *Comput. Electr. Eng.* **2020**, *83*, 106574. [CrossRef]
32. Alreni, A.; Momcheva, G.; Pavlov, S. Voronoi Diagrams and Perlin Noise for Simulation of Irregular Artefacts in Microscope Scans. In Proceedings of the 15th International Joint Conference on Biomedical Engineering Systems and Technologies (Bioimaging), Vol 2, Online, 9–11 February 2022; SCITEPRESS: Setúbal, Portugal, 2022; pp. 117–122. [CrossRef]
33. Li, Y.; Cui, F.; Li, L. An integrated optimization model for the location of hydrogen refueling stations. *Int. J. Hydrogen Energy* **2018**, *43*, 19636–19649. [CrossRef]
34. Yang, G.; Jiang, Y. Siting and sizing of the hydrogen refueling stations with on-site water electrolysis hydrogen production based on robust regret. *Int. J. Energy Res.* **2020**, *44*, 8340–8361. [CrossRef]
35. Cao, F.; Meng, Q.; Miao, P.; Li, Y. Optimal substation planning based on improved weighted voronoi diagram and genetic algorithm. *Power Syst. Technol.* **2015**, *39*, 511–516. [CrossRef]
36. Hou, H.; Tang, J.; Wang, Y.; Xia, X.; Wang, F.; Hu, P.; Xie, C. Layout planning of electric vehicle charging stations in urban areas. *Power Syst. Prot. Control* **2022**, *50*, 181–187. [CrossRef]
37. Yan, G.; Liu, H.; Han, N.; Chen, S.; Yu, D. An Optimization Method for Location and Capacity Determination of Charging Stations Considering Spatial and Temporal Distribution of Electric Vehicles. *Proc. Chin. Soc. Electr. Eng.* **2021**, *41*, 6271–6283. [CrossRef]
38. Liu, F. Design of Human Motion Training Motion Capture Model Based on Improved PSO Algorithm. In Proceedings of the 1st IEEE International Conference on Applied Intelligence and Sustainable Computing, ICAISC 2023, Dharwad, India, 16–17 June 2023.
39. Choulli, I.; Elyaqouti, M.; Arjdal, E.; Ben Hmamou, D.; Saadaoui, D.; Lidaighbi, S.; Elhammoudy, A.; Abazine, I. Hybrid optimization based on the analytical approach and the particle swarm optimization algorithm (Ana-PSO) for the extraction of single and double diode models parameters. *Energy* **2023**, *283*, 129043. [CrossRef]
40. Gao, H.; Liu, J.; Shen, X.; Xu, R. Optimal Power Flow Research in Active Distribution Network and Its Application Examples. *Proc. Chin. Soc. Electr. Eng.* **2017**, *37*, 1634–1644. [CrossRef]
41. Low, S.H. Convex relaxation of optimal power flow—Part i: Formulations and equivalence. *IEEE Trans. Control Netw. Syst.* **2014**, *1*, 15–27. [CrossRef]
42. Song, Z.; Hu, Y.; Guo, H.; Ma, J.; Song, B.; Xu, M.; Liu, Z. Optimal Design Method for the Partitioning of OLTC-Inverter Control Parameters in Distribution Stations with High-proportion Residential Photovoltaics. In Proceedings of the 2022 International Conference on Innovations and Development of Information Technologies and Robotics, IDITR 2022, Chengdu, China, 27–29 May 2022; pp. 43–49.
43. Dabaghi-Zarandi, F.; Behjat, V.; Gauvin, M.; Picher, P.; Ezzaidi, H.; Fofana, I. Power Transformers OLTC Condition Monitoring Based on Feature Extraction from Vibro-Acoustic Signals: Main Peaks and Euclidean Distance. *Sensors* **2023**, *23*, 7020. [CrossRef]
44. Huang, J.; Geng, Y.; Jin, Q.; Chen, X.; Yan, J.; Geng, Y. The Influence of the Dispersion in Pre-arcing Time of Vacuum Circuit Breakers on the Controlled Switching of Capacitor Banks. In Proceedings of the 6th International Conference on Electric Power Equipment—Switching Technology, ICEPE-ST 2022, Seoul, Republic of Korea, 15–18 March 2022; pp. 206–211.
45. Zein, H.; Saodah, S.; Utami, S.; Wachjoe, C.K. Static VAR Compensation Capacity for Bus Voltage Setting in Electric Power Systems. In Proceedings of the 4th International Conference on Technology and Policy in Energy and Electric Power, ICT-PEP 2022, Jakarta, Indonesia, 18–20 October 2022; pp. 1–6.

46. Liu, S.; Wei, C.; Wang, H.; Yang, W.; Zhang, J.; Wang, Z.; Zhao, W.; Lee, P.S.; Cai, G. Processable nanoarchitectonics of two-dimensional metallo-supramolecular polymer for electrochromic energy storage devices with high coloration efficiency and stability. *Nano Energy* **2023**, *110*, 108337. [CrossRef]
47. Qian, Y.; Lyu, Z.; Zhang, Q.; Lee, T.H.; Kang, T.K.; Sohn, M.; Shen, L.; Kim, D.H.; Kang, D.J. High-Performance Flexible Energy Storage Devices Based on Graphene Decorated with Flower-Shaped MoS_2 Heterostructures. *Micromachines* **2023**, *14*, 297. [CrossRef] [PubMed]
48. Jin, B.; Liu, Z.; Liao, Y. Exploring the Impact of Regional Integrated Energy Systems Performance by Energy Storage Devices Based on a Bi-Level Dynamic Optimization Model. *Energies* **2023**, *16*, 2629. [CrossRef]
49. Zhou, L.; Peng, W.; Ma, L.; Yu, W. Orderly Charging and Discharging Scheduling of DC V2G Charging Pile Considering Load Balance of Electricity Reticulation. In Proceedings of the 1st IEEE International Conference on Applied Intelligence and Sustainable Computing, ICAISC 2023, Dharwad, India, 16–17 June 2023.
50. Jiang, Y.; Yang, G.; Zhu, Z. Wind-Hydrogen-Electricity Coupled Network Planning Considering Traffic Flow Capture. *Autom. Electr. Power Syst.* **2021**, *45*, 19–28. [CrossRef]
51. Kashem, M.A.; Ganapathy, V.; Jasmon, G.B.; Buhari, M.I. A novel method for loss minimization in distribution networks. In *DRPT2000. International Conference on Electric Utility Deregulation and Restructuring and Power Technologies, Proceedings (Cat. No.00EX382)*; IEEE: Piscataway, NJ, USA, 2000; pp. 251–256.
52. Song, Y.; Hu, X. Learning-based demand-supply-coupled charging station location problem for electric vehicle demand management. *Transp. Res. Part D Transp. Environ.* **2023**, *125*, 103975. [CrossRef]
53. Wang, M.; Dong, X.; Zhai, Y. Optimal Configuration of the Integrated Charging Station for PV and Hydrogen Storage. *Energies* **2021**, *14*, 7087. [CrossRef]